Characterisation of flame surface annihilation events in self excited interacting flames

Nicholas A. Worth, James R. Dawson

Department of Energy and Process Engineering, Norwegian University of Science and Technology, N-7491, Trondheim, Norway

Abstract

This paper investigates the non-linear flame dynamics of two interacting, premixed, V-shaped flames by characterising the two-dimensional topology of flame annihilation events when the separation distance, S, between them is reduced and large-scale flame merging occurs. The equivalence ratio was varied to promote self-excited oscillations, with the oscillation frequency, heat release phase, and stability limits shown to be dependent on S. High-speed OH-PLIF measurements show that these changes are correlated with the break-up of the shear layers into structures that lead to large-scale flame annihilation events. In isolated flames the shear layers break-up independently, but as S is reduced the shear layers combine leading to large-scale flame merging resulting in the roll up of a single large-scale vortex structure altering the flame annihilation events compared with the case of isolated flames. A flame front event tracking algorithm is developed to characterise the two-dimensional topology and identify the number and spatial location of flame front annihilation events, which shows a strong correlation between these events and the fluctuating heat release rate. Compared with stable flames for the same S, it is found that self-excited instabilities do not significantly increase the number of annihilation events but rather affects their spatial distribution and phase within the oscillation cycle. It is also shown that flame merging significantly increases the probability of flame front annihilation events which alters the phase of the fluctuating heat release rate.

Keywords: Turbulent premixed flames, combustion instability, flame-flame interactions, multiple flames, flame front tracking, annihilation events

1. Introduction

It is well recognised that low emission lean burn concepts for gas turbine combustors are susceptible to self-excited thermo-acoustic oscillations. These occur due to positive feedback between unsteady pressure, flow, and heat release oscillations, which results in the linear growth of instabilities followed by saturation into limit-cycle oscillations due to non-linear effects [1]. The non-linear response of the flame is usually associated with the mutual annihilation of flame fronts which has been observed in both laminar and turbulent premixed flames [2, 3, 4, 5]. Nevertheless, predicting limit-cycle amplitudes remains a challenge which is at least, in part, due to a limited understanding of the dynamics of flame annihilation events and how they are correlated with the non-linear response in turbulent flames.

It is well known that turbulent premixed flames exhibit local mutual flame annihilations which modify the flame surface area and cause large fluctuations in the heat release rate [6, 7]. Recently, it has also been shown that local flame annihilations act as local sources of sound generation [8]. Flame annihilation events specifically describe the collision of flame surfaces, which annihilates the flame at the contact point, and alters the flame topology. This results in pocket formation that then in turn lead to large fluctuations in the heat release rate. It therefore also describes the collision of flame surfaces caused by the roll-up of vortex structures [3].

Variations in the flame surface area can be rigorously studied using flame topologies [6, 7]. Mutual annihilation of impinging flame fronts as a mechanism for pocket formation was first studied by Chen et al. [6] using 2D Direct Numerical Simulations (DNS). Three distinct topologies were identified: (1) Flame Channel Closing (FCC) which involves direct quenching, as two flame fronts propagate into one another forming cusps

Email address: `nicholas.a.worth@ntnu.no` (Nicholas A. Worth)

either side of the pinching location and resulting in an isolated region of unburned gas; (2) Cusp Recovery (CR) involving the rapid burn off of elongated regions of reactants; and (3) Pocket Burn-Out (PBO), where pockets of unburned reactants that are isolated through mechanisms such as FCC are burned off. A more recent study using 3D DNS [7] showed that changes to the flame topology which result in cups formation and pocket burnout events can significantly affect the balance of flame surface area production and destruction, and therefore the heat release rate.

In the case of combustion instabilities, the resulting unsteady flow has long been associated with the formation of large-scale vortex structures and their interaction with the flame [9, 10, 11, 12, 13, 14, 15] including observations of flame annihilation [3, 16]. In laminar premixed flames both theory and experiments have shown annihilation events to be the dominant generation mechanism of pressure disturbances and the source of non-linearity [2, 17]. This is often postulated to also be valid in turbulent flames, for example when modelling flame sheet kinematics using a G-equation approach only large-scale flame motions due to flow unsteadiness are considered [18, 19]. It is, however, not understood whether annihilation events which inherently arise from turbulent-flame interactions contribute to the non-linear flame response given that in intense shear flows they can occur over a range of scales. Furthermore, despite direct observations of flame annihilation events in turbulent flames [3, 16] the spatial and temporal characteristics of large-scale annihilation events due to flow unsteadiness has not yet been investigated.

In this paper we use high-speed OH-PLIF to analyse the 2D flame geometry by extending the topological approach of Chen et al. [6], Griffiths et al. [7] to combustion instabilities. This provides a more generalised and scale-independent methodology to investigate the role of flame annihilation events on non-linear flame dynamics in more detail over the resolvable scales of the measurements. An experimental configuration of two bluff body stabilised turbulent premixed flames with varying separation distance, S, is investigated. Previously, a similar configuration with acoustic forcing was used to study the effect of S on the mean flame shape and vortex-flame dynamics, emphasising the role of flame merging and forcing amplitude on the non-linear flame response [20]. In this paper, we conduct a series of experiments similar to Worth and Dawson [20] but for self-excited flames.

The paper begins by detailing the apparatus, experimental methods, and flame front event tracking algorithm. The self excited oscillations are first characterised through pressure and global OH* measurements, demonstrating the oscillation frequency and stability dependence on S. The flame front events are then characterised in the following sections, and finally linked to the flame response before some conclusions are drawn. The classification of topology in the current study provides a way to link physical events to the modification of flame surface area, and therefore this approach allows us to physically quantify the effect of flame-flame interactions, rather than simply observing that annihilation events may occur.
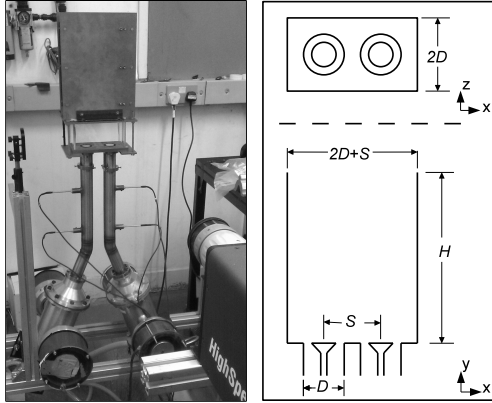
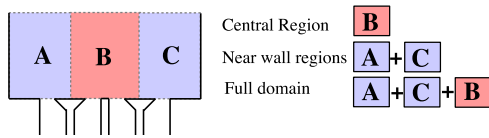Figure 1: Experimental setup image and schematic showing burner scaling

Figure 2: Regions of interest for integrated FSD and event tracking

2. Experimental Methods

2.1. Burner and instrumentation

The experimental apparatus shown in fig. 1 is similar to the setup in Worth and Dawson [20], but some of the key differences to achieve self-excited flames will be briefly reported here. Two identical premixed flames are placed side by side in a rectangular enclosure. The inlet ducts have a diameter of $D = 35$mm, with a 25mm centrally located conical bluff-body giving a blockage ratio of 50%. The separation distance between the flames was varied, and spacings of $S = 1.14D$, $1.43D$ and $2.00D$ were investigated, where S is defined as the distance between bluff-body centres (see fig. 1). To obtain self-excited instabilities the enclosure geometry was extended in the present work to a height of $H = 350$mm. An 85mm section of the enclosure was quartz to allow optical access. One of the enclosure sidewalls was adjusted for each S to maintain a constant wall spacing.

Air and fuel flow rates were independently controlled for each of the flames using four mass flow controllers.The controllers have measurement ranges of 1000 litres per minute (lpm) for air and 100 lpm for methane, with an accuracy of ±0.8% of the reading plus ±0.2% of the full scale. The bulk reactant exit velocity was set to 10ms^{-1} which gave a Reynolds number of 1.7×10^4 based on bluff-body diameter. The equivalence ratio was varied between $\phi = 0.64$ to 1.0 in order to promote self-excited oscillations.

Two dynamic pressure transducers were flush mounted on each inlet duct at two upstream locations in order to calculate the velocity fluctuation magnitude using the two-microphone technique. The sensors have a sensitivity of 4.29μV/Pa, and a frequency response of 30kHz, and the signals were amplified and filtered prior to recording. Global chemiluminescence measurements were made using a photomultiplier tube with a UV bandpass filter (300-325nm). Data was acquired at 10kHz over 3.2s, and digitised, producing a frequency resolution of 0.3Hz. Spectral analysis was used to assess the complex velocity amplitude, $A = u'(f)/\overline{U}$, and global heat release, $q'(f)/\overline{Q}$. Microphone and PMT measurements were repeated 3 times to improve convergence.

2.2. High Speed OH-PLIF

In order to extract flame front contours for tracking time-resolved OH-PLIF measurements were performed. The imaging setup is the same as used by Worth and Dawson [20], and therefore a complete description will not be presented here, although the basics of the setup will be recapped. The PLIF system consisted of a 15W pump laser and a high-speed dye laser operated at 5kHz. A series of optics were used to produce a thin 40mm high sheet whose path traversed the centres of both bluff bodies. Imaging was performed using a high-speed CMOS camera (1024^2 pixel resolution) coupled with a high-speed two-stage intensifier, fitted with a UV lens and OH filter (300-325 nm). A total of 5400 images were obtained for each case.

After correcting for beam profile inhomogeneities the flame surface density (FSD) was computed following a similar approach to Balachandran et al. [3], using an interrogation window size of 5 pixels which, based on the field-of-view results in a spatial resolution of the order of 1mm. The FSD is the integrated local flame length over the interrogation window area. The limited illumination power required separate measurements to be made in the lower and upper halves of the combustor, with an overlap of 10mm. FSD images were then stitched together to cover the entire domain, with the mean of upper and lower contributions used in the overlap region. During the analysis the FSD contribution and flame front events from the full domain are divided by region in §3.2.3 according to the schematic presented in fig. 2. The phase average FSD fields are largely used in the present work to help give context to the location of the flame front tracking results, presented in §3.

Weighted phase images were calculated from the stitched FSD images using a similar approach to Hauser
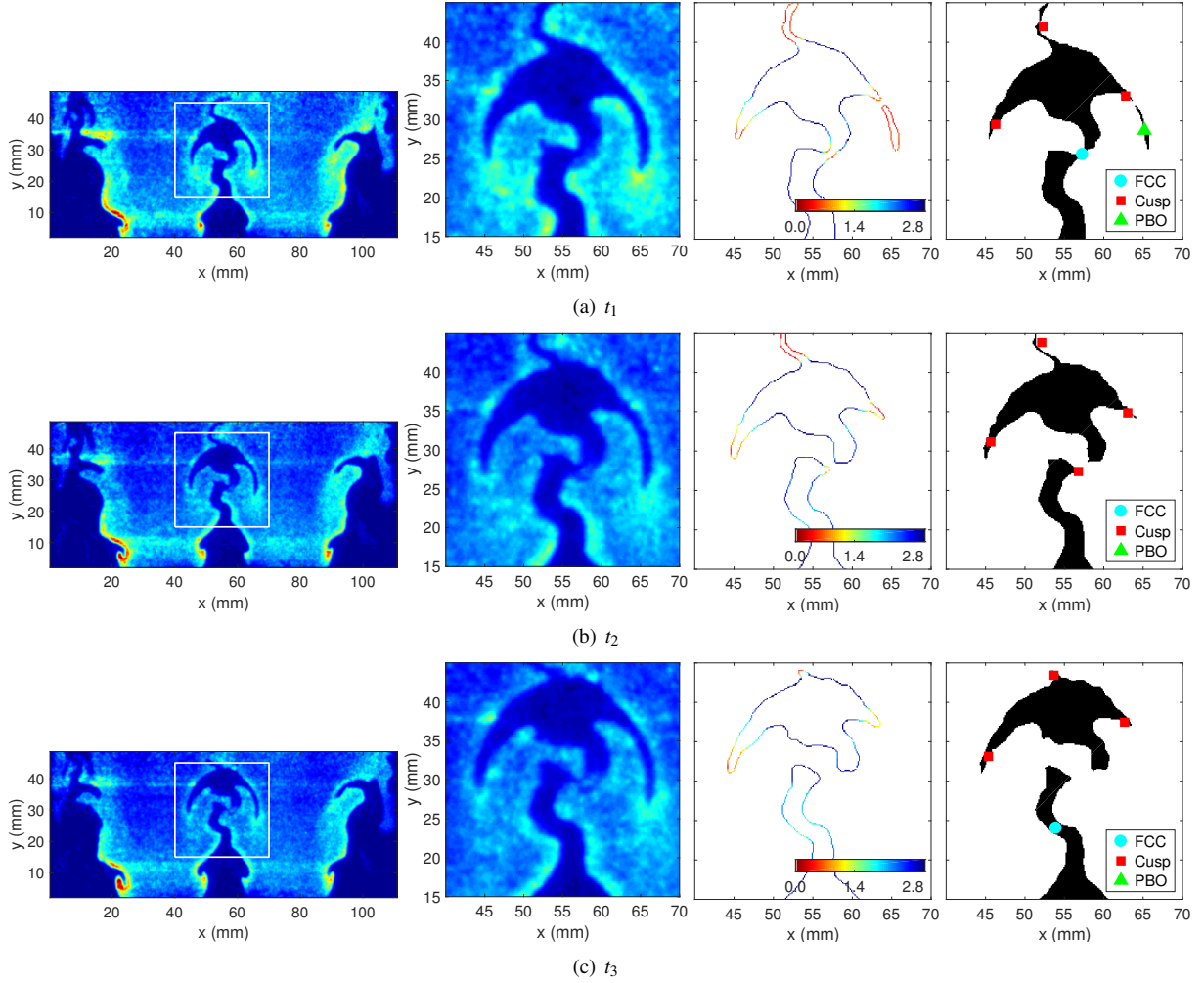
3

Figure 3: Example of event tracking algorithm on three image frames. In each subplot: *Left*, OH PLIF full field view, with zoom window highlighted; *Centre Left*, OH PLIF enlarged window; *Centre Right*, Detected edge regions coloured by distance along a vector normal to the opposing edge, d_n; *Right*, Identified potential events are marked over the progress variable map. (*Colour online*).

et al. [21]. An FFT based method was used to calculate the amplitude and relative phase of fluctuation for each pixel in the phase averaged FSD images at the self-excitation frequency. The brightness of the phase images was then weighted by the amplitude images, so that the image colour indicates phase angle and brightness indicates fluctuation magnitude. Through this weighting the phase is only discernible in image regions with a significant fluctuation amplitude, providing a useful way of understanding the spatio-temporal variation of heat release oscillations.

2.3. Analysis of flame front annihilation events

In the premixed turbulent methane flames studied in the current investigation, flame front annihilation events

are observed to occur primarily through the advection of unburned reactants, where opposing flame fronts are brought together. As the $Le \approx 1$ local extinction events are not prevalent in regions of high local strain[22]. Based on the spatial resolution and the thresholding used in event identification discussed in the next section, the smallest events captured are of the order of 1mm. Flame front annihilation events can be identified manually by observation from the time-resolved OH-PLIF data. Figure 3 shows three instances in a typical OH-PLIF time-series, in which several annihilation events can be observed. The zoomed window shows the pinch-off of the large central merged vortex structure, resulting in a large scale FCC event. Large cusps are also clearly visualised in the bluff body re-circulation
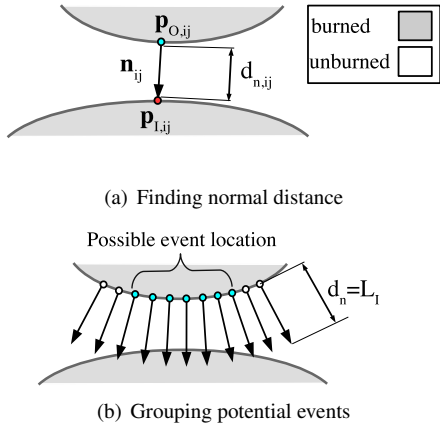
4

(a) Finding normal distance

(b) Grouping potential events

Figure 4: Algorithmic identification of potential events by examination of closely spaced flame fronts. (a) extrapolation along contour normal, $\mathbf{n}_{ij}$, in order to find the normal intersection distance, $d_{n,ij}$, at each pixel location. (b) Identification of a possible event location through a group of neighbouring pixels along a single contour whose normal intersection distances are less than a prescribed threshold distance.

(a) Flame Channel Closing (FCC)
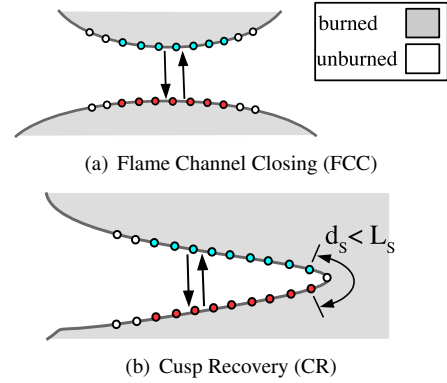

(b) Cusp Recovery (CR)

Figure 5: Classification of potential events. (a) Flame Channel Closing events are classified as potential event locations which reference each other and are either on different contours, or are a significant distance from each other on the same contour. (b) Cusp events are classified as potential event locations which self-reference, or reference another potential event which is closely located along the same contour.

zones, and also above the crescent shaped region of unburned gasses from the pinch-off event in the previous cycle. The present investigation seeks to characterise these mechanisms in both the stable and self-excited cases following the convention defined by Chen et al. [6], by identifying and separately classifying events as flame channel closing (FCC), cusp recovery (CR), or pocket burnout (PBO).

Before the FCC event the two adjacent flame fronts are observed advancing towards each other, reducing their mutual separation distance as measured along a vector normal to the flame front. It is this observation that can be used to algorithmically identify flame front sections (by thresholding on this normal distance) which are likely to undergo mutual annihilation. By tracking the location of potential events, and monitoring their sudden absence (due to an annihilation event) it is possible to algorithmically characterise not only the type of event, but also the frequency, and spatial distribution of these from the OH-PLIF data. The algorithm used is described in two sections: first on the identification of potential events; and second on their classification and tracking.

Before the method is introduced, two important caveats must be noted which relate to the use of planar imaging. Firstly, we can only measure planar intersections of the flame surface and cannot capture out-of-plane motions of the flame. In the absence of swirl, the in-plane velocity fluctuations are significantly greater than the out-of-components. We therefore expect a ma-

jority of events to occur from the in-plane motions. However, the current algorithm cannot distinguish between events resulting from either the in-plane or out-of-plane propagation of flame fronts. Although out-of-plane events may be non-negligible they are less probable. The second caveat is that for closely spaced flames axisymmetry is destroyed in the interaction region. Therefore care must be taken when considering planar measurements of flame surface area in the context of global measurements of the fluctuating heat release rate using a PMT.

It is generally acknowledged that there are weaknesses with planar measurements that cannot be addressed without full three-dimensional diagnostics, but such capabilities are not currently available.

2.3.1. Identification of potential events

The first stage in algorithmic classification is the identification of *potential* events, which are detected in the current algorithm by the presence of closely spaced flame fronts and isolated flame pockets. These regions are tracked, and annihilation events inferred to occur from these tracked sequences. The current section details the implementation of the algorithm, and an assessment of its accuracy.

The OH-PLIF images were post-processed to correct for mean beam profile inhomogeneities, including both the Gaussian beam intensity distribution and the development of beam thickness across the field of view. Gaussian smoothing was applied with a kernel width of 3 pixels to remove noise before converting the images to binary using an intensity thresholding based algorithm.
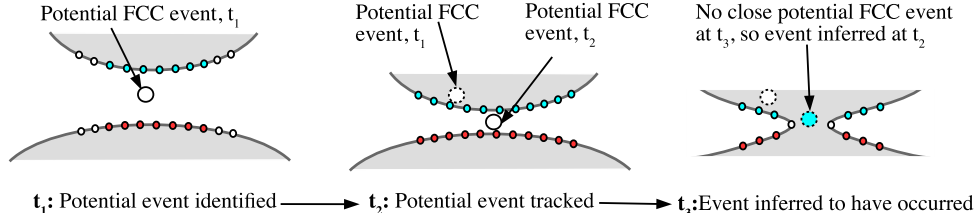
Figure 6: Tracking of potential events. A potential FCC event is identified through closely spaced flame front normals, and tracked across several frames. The potential FCC event is first identified at time t_1 due to closely spaced groups of pixels who's normal intersection distance is below the threshold level. Another potential FCC event is identified at time t_2, and given their physical proximity the two potential FCC events are linked, and the event is tracked. At time t_3 an FCC event cannot be identified, and therefore through the absence of a previously tracked event, the actual event is inferred to have occurred at time, t_2.

The thresholding algorithm assigned binary values of the progress variable c to define regions of fresh mixture $c = 0$, or burnt gases $c = 1$, after which a Canny edge detection algorithm was employed to find a total of N_j instantaneous edge contours on each image.

The spatial location of the edge contours were smoothed through the application of a 5 pixel wide top-hat filter. Each edge contour contains N_i pixel locations. The image location, $\mathbf{p}_O$, of the ith pixel on the jth edge contour is denoted as, $\mathbf{p}_{O,ij}$. A normal vector, $\mathbf{n}_{ij}$, was calculated at each pixel location, based on the local gradient of the contour over a local neighbourhood of 5 pixels. The normal orientation was set to face in the direction of the unburned gasses. Linear extrapolation along the normal vector was used to find the intersection of the normal vector with the nearest flame edge, which was then stored as the point, $\mathbf{p}_{I,ij}$. The normal distance between these flame front locations, $d_{n,ij} = \sqrt{(\mathbf{p}_{O,ij} - \mathbf{p}_{I,ij}) \cdot (\mathbf{p}_{O,ij} - \mathbf{p}_{I,ij})}$, and the original and intersection locations ($\mathbf{p}_{O,ij}$ and $\mathbf{p}_{I,ij}$) are stored, with the latter used during the cross referencing method as part of the classification section of the algorithm. The calculation of the normal distance is shown schematically in fig. 4(a).

Using the stored normal distances, possible event locations can be identified as connected edge pixel locations where the intersection distance is less than a given threshold value, as shown schematically in fig. 4(b). A threshold distance of $L_I = 1.8$mm was selected to account for the maximum observed flame front normal velocity, allowing closely spaced flame fronts to be identified in multiple frames. This ensures that all possible events are included, as closely spaced flame fronts can be identified before they have time to propagate into each other resulting in annihilation events, based on the sampling frequency and advection velocities. Given that the occurrence of flame front annihilation events must be inferred from the disappearance of such closely spaced sections, the identification of these sections in several frames does not significantly affect the results, based on a sensitivity analysis of this threshold (shown in §2.3.3).

This approach is based on locating clustered regions of closely separated flame fronts. However, sudden variations of the distance, d_n, along the flame front (due to the sometimes highly contorted flame structure) can lead to breaks in closely separated flame front sections, resulting in multiple instances of the same sections being identified. This problem is significantly reduced by smoothing the calculated normal distances along the flame front using a top hat filter with a kernel width of 9 pixels, thereby linking close structures. Groups containing less than 13 connected pixels were removed to improve sensitivity to noise. Based on these constraints the smallest length scale of events that can be detected are of the order of 1mm.

2.3.2. Potential event classification

Of the three different types of event described by Chen et al. [6] PBO events can be readily classified as flame fronts surrounding small isolated regions of unburned gas. An assessment of the size of the regions is available through the binary progress variable field directly, without the need to examine normal intersection distances. A threshold value of $A_P = 15$mm^2 was chosen to identify these regions. Detached pockets of reactants above this size are treated in the same way as the main flame. Although PBO events occur on both the reactant and product sides of the flame as shown in [7], we can only capture reactant side events using OH-PLIF due to signal contamination in the post-flame region. Detached pockets of reactants above this size are treated in the same way as the main flame.

In order to differentiate between FCC and CR events a cross referencing scheme was applied based on the previously stored normal intersection locations of each

(a) Normal distance threshold, L_I (b) Pocket size threshold, A_P (c) Contour separation threshold, L_S
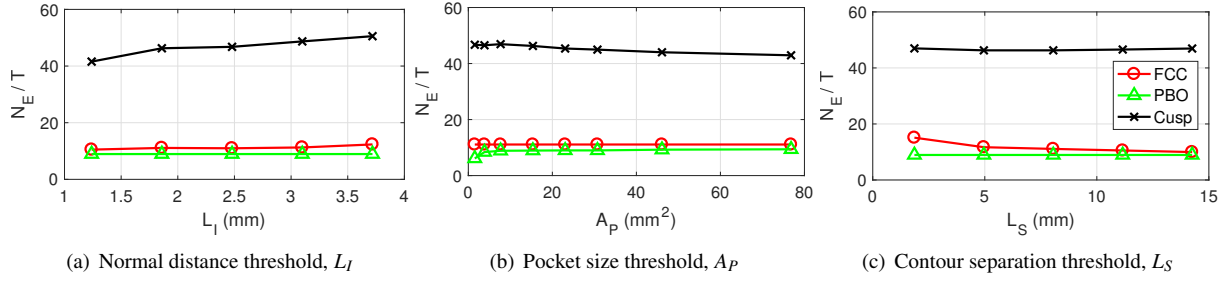
Figure 7: Parametric study of threshold quantities showing the results are largely insensitive to the chosen threshold values.

pixel. The normal intersection location of each grouped edge section pixel was compared with the location of all other flame front groups. If the intersection locations are found to predominantly coincide with another edge section group then these sections groups are tagged together, as shown in fig. 5. If the tagged sections lie on the same flame front contour the distance between them along the contour, d_S, is measured. A distance threshold of $L_S = 8$mm was introduced to separate closely separated events. CR events are defined as sections which predominantly reference themselves or a close neighbouring section on the same edge contour $d_S < L_S$, as shown in fig. 5(b). FCC events are defined as those referencing sections which are either a significant distance away along the same flame contour ($d_S > L_S$), or are located on a separate contour, as shown in fig. 5(a). For each potential event the average location is defined as the average of all the pixel locations from all contours in group, G, calculated as $\overline{\mathbf{p}_{O,G}} = \frac{1}{N_i N_j} \sum_1^{N_j} \sum_1^{N_i} \mathbf{p}_{O,ij} \in G$, and the potential event size is calculated as the total number of pixels from all grouped contours.

As described previously, the approach used in the current work tracks *potential* events in order to infer when an *actual* event occurs. As the velocity field is not known, a more simplistic tracking approach must be used. The spatial locations of all potential events identified at each instance in time, are compared with the spatial locations of potential events at each subsequent time step, and the distance between events evaluated as d_E. A separation threshold, $L_E = 4$mm was selected to account for the maximum combined advection and propagation velocity of the potential events. Potential events which are closely spaced ($d_E < L_E$) are paired under the assumption that both instances correspond to the same potential event, and therefore, the event has not yet occurred. When a potential event can no longer be tracked (matched to a subsequent instant in time), then it is inferred that the event has occurred, and the last known location of the event is marked. The identifica-

tion of an FCC event in this manner is shown schematically in fig. 6.

The identification algorithm is demonstrated on the experimental data in fig. 3. OH-PLIF images of the full field of view are shown at three instances in time on the left hand side of the figure, with a white box indicating a region selected for enlargement. The enlarged OH-PLIF image is shown for each time instance on the centre-left, together with the flame front contours on the centre-right images, which have been coloured by the normal intersection distance, d_n. Possible event locations can be readily identified as connected edge pixel locations with small intersection distances (those in which the contour colour varies from red to green). Plots on the right hand side show the potential event locations. The potential event markers are coloured by type, demonstrating the ability of the scheme to correctly identify the three described event types. The absence of the central FCC event and right hand side PBO event at t_2 in fig. 3(b) will result in actual events being recorded.

Erroneous event classification, event classification changes between consecutive frames, or when closely spaced flame fronts do not actually result in an annihilation event will introduce uncertainty into the results. Imperfect assignment of values for the progress variable will result in different shaped regions between the OH-PLIF images and actual flame surface calculation which also contribute to uncertainty. As a consequence this may introduce a small phase shift in the temporal identification of events the FSD will also exhibit the same phase shift. Such errors in the phase shift are much smaller than the phase average resolution and therefore have a negligible effect on results presented. In order to assess the accuracy of algorithm and its sensitivity to the various chosen thresholds, in the following 2 sections a parametric study is first conducted, before a comparison is made against manually observed FCC events.

(a) Manually observed FCC events
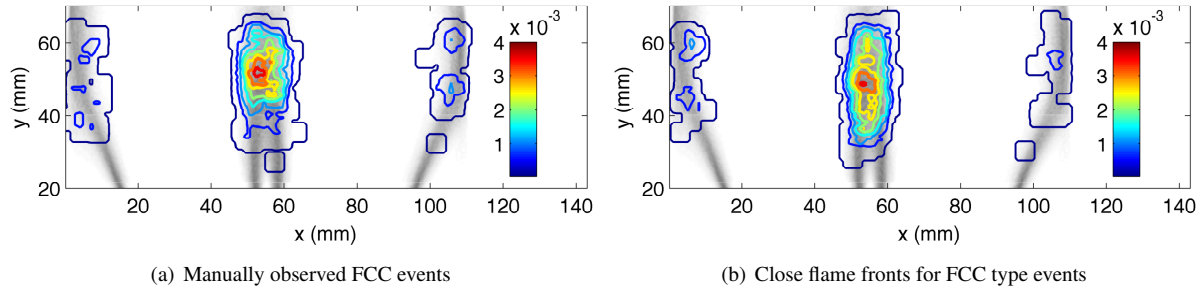
(b) Close flame fronts for FCC type events

Figure 8: Comparison of the JPDF distribution of manually observed events and algorithmically identified FCC events. The JPDFs were constructed from a 500 frame image sequence, for the unforced $S = 1.14D$ case. To improve interpretation of the figure the underlying mean flame structure also shown through contours of the mean FSD using a grey colour map. (*Colour online*).

2.3.3. Threshold dependence of results

In order to quantify the effect of the threshold parameters on event identification a parametric study was conducted. The stable $S = 1.14D$ case was used ($\phi = 0.7$) with default threshold values of $L_I = 1.8$mm, $L_S = 8$mm and $A_P = 15$mm^2. The total number of each event, N_E, plotted in fig. 7 is averaged over a time period of $T = 2.78$ms. This time period corresponds to the time for a single oscillation cycle at a frequency $f = 360$Hz, which although somewhat arbitrary for the stable case, permits later comparison with the self-excited data.

Figure 7(a) shows that FCC and Cusp events have a weak dependence on L_I. As this threshold is increased more potential events are stored, resulting in a higher number of tracked events. Under ideal tracking conditions increasing this threshold level should not increase the number of events identified, but rather it should result in the same events being identified earlier and tracked for longer. Therefore, the weak positive slope for the number of events is a result of errors in the tracking algorithm. However, it should be stressed that the dependence is slight, and doubling the threshold from 1.8 to 3.6mm only results in an increase of approximately 10%. To minimise tracking losses a relatively low threshold of $L_I = 1.8$mm was chosen, at which point the number of events identified is relatively stable.

Figure 7(b) shows that over a threshold value of around $A_P = 3.8$mm^2 the number of PBO events remains approximately constant, with an order of magnitude change in the threshold value resulting in a variation of around 5%. Therefore, the tracking of this event type can be considered reasonably accurate. It is interesting to note that as the threshold size is increased the number of cusp events is reduced. This is a result of the classification definitions, where if an isolated region of unburned gas is classified as a potential PBO

event subsections of that region can no longer be classified as cusps. Therefore, to minimise tracking losses and loss of cusp type events a relatively low threshold of $A_P=15$mm^2 was chosen.

Finally the effect of the contour separation distance threshold, L_S, on the number of events is shown in fig. 7(c). As expected, increasing L_S results in the classification of more cusp as opposed to FCC events. However, for threshold values $L_S > 5$mm the change in the number of FCC events is slight (doubling the threshold results in a change of around 8%). Therefore, the threshold value was chosen as $L_S = 8$mm; a value which removes the majority of cusp-like events, but also permits FCC events relatively close to a cusp.

2.3.4. Assessment of the algorithm accuracy

Finally, in order to assess the performance of the current algorithmic identification approach a comparison was made against manually observed FCC events. Comparisons were made over 500 frames for the upper half of the unforced $S = 1.14D$ case, with JPDFs of event probability shown in Fig. 8. Figures. 8(a) and (b) both show high probabilities in the interacting region between the two flames with much lower probabilities near the walls. The location of the peak probability is around y=50mm in the manually observed case, with the algorithmically identified cases producing a more elongated distribution, albeit with similar peak height and contour levels. Differences in the distributions are expected to result from errors in the algorithmic approach, falsely identifying a number of events closer to the flame base.

The accuracy of the algorithm may also be influenced by thresholding, producing differences between the observed flame fronts in the OH-PLIF data and the binarised progress variable. Furthermore, although the manual identification of events may generally be less prone

8

(a) Velocity amplitude response

(b) Frequency response

(c) Phase difference between heat release and velocity fluctuations

(d) Phase difference between velocity oscillations on left and right hand side flames
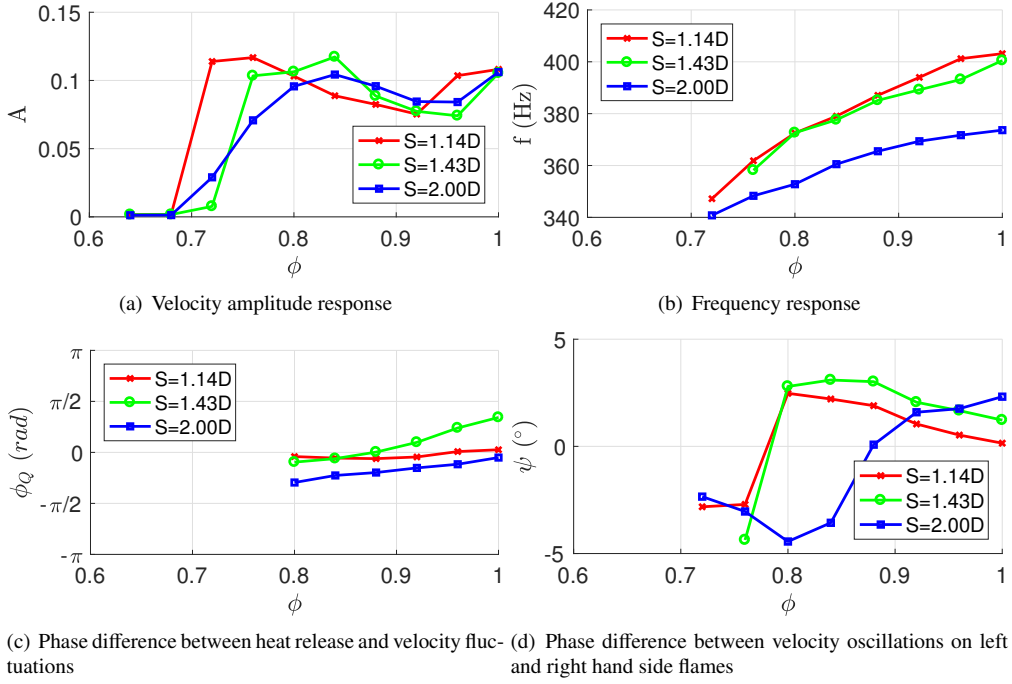
Figure 9: Characterisation of self-excited fluctuations with varying equivalence ratio at three flame separation distances.

to error, it is dependent on the subjective judgement of the user; a difference which may both account for some of the observed errors and which makes the use of an algorithmic method preferable. While the current algorithmic identification and tracking of flame front events may be imperfect, this comparison demonstrates that the method is still suitable for quantifying the spatial location and approximate number of events, allowing differences between cases to be assessed for the first time with direct reference to these flame front events.

3. Results and Discussion

In the following section the self-excited fluctuations are first characterised using simultaneous PMT and two-microphone measurements at three flame separation distances, before analysing the results of the flame front tracking algorithm.

3.1. Characterisation of Self-Excited Fluctuations

Figure 9(a) shows the effect of ϕ on the velocity oscillation amplitude. The amplitude response of both flames was measured and found to be very similar therefore the average is presented. The equivalence ratio corresponding to the onset of self-excited instabilities and the slope of the limit cycle amplitude with varying ϕ is highly dependent on S. For the merged flame cases

$(S = 1.14D$ and $1.43D)$ a steeper slope of the limit cycle amplitude response is observed, whereas for flames that are almost isolated at $S = 2.00D$, a more gradual slope is seen. Only small variations in the limit cycle amplitudes between different S are also observed for higher equivalence ratios. The saturated response of the forced configuration at a similar frequency also showed similar amplitude levels between cases at different separation distances [20], therefore the observed similarity in the self-excited amplitude response is somewhat expected. The amplitude response is discussed further in §3.2.3. Overall these results show that the flame stability limits and the effect of ϕ on the limit-cycle amplitude is correlated with S, and that the effect of S on the stability limits is consistent with the behaviour of self-excited flames with varying S in annular geometry [16].

The frequency response also exhibits a strong S-dependence due to modification of the flame structure. Fig. 9(b) plots the variation of the instability frequency with ϕ, for magnitudes of oscillation $A > 0.01$. The instability frequency ranges from $f = 340 - 400$Hz for all S corresponding to the same combustor modes reported previously [3, 20]. For all S, the variation of the instability frequency with ϕ shows similar trends. However, a distinct frequency shift is observed between the merged and unmerged flames cases. The merged flame cases, $S = 1.43D$ and $1.14D$, exhibit a frequency in-
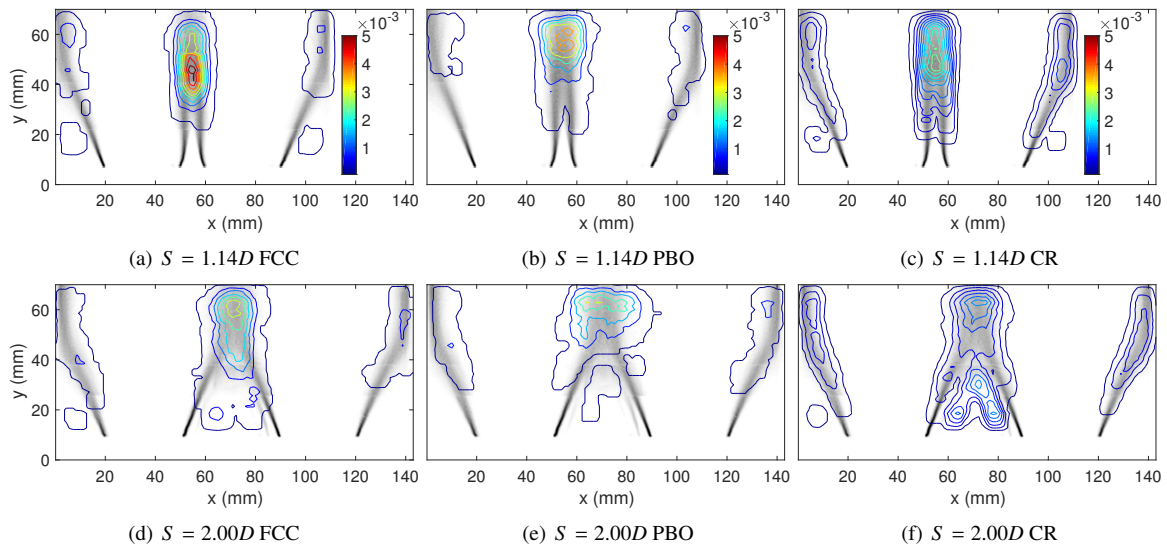
Figure 10: JPDF of different flame front events on stable flames ($\phi = 0.7$) showing the effect of varying separation distance. Probability densities are indicated by colour bar, with the same scale used for all distributions. The mean FSD is plotted in grey scale to help provide context to the event tracking results. (*Colour online*).

crease between $10 - 25$Hz relative to the isolated flame case, $S = 2.00D$. As ϕ is increased so is the flame speed and the flame temperature, the former will predominantly affect the phase whereas the latter results in an increase in the mean gas temperature and therefore the speed of sound. Since the acoustic modes remain the same, we identify several possible mechanisms that may alone or in combination result in the observed frequency shift at a given operating point. These are: *i)* a change in phase; *ii)* a change in the unsteady heat loss; *iii)* large-scale modification to the flame structure.

The delay calculated from the phase difference between q' and u' is plotted in fig. 9(c). Overall, distinct changes are observed for different S. Both $S = 1.43D$ and $S = 2.00D$ cases show similar trends exhibiting a small but finite increase with ϕ but with approximately constant phase shift relative to each other. However, the phase response in the case of the fully merged flames, $S = 1.14D$, is comparatively flat. The relatively flat response of $S = 1.14D$ indicates that the degree of flame-merging is likely to be an important factor in the flame response. As shown in previous work [20] the flame merging for $S = 1.43D$ occurs near the top of the flame brush, but for $S = 1.14D$ case the merging occurs further upstream. This affects both the magnitude and phase of q' locally. Changes to the flame structure may also affect the unsteady heat loss, unfortunately we did not measure the wall temperatures in these experiments. These changes may, at least in part, explain the changes to the phase and frequency trends observed.

We can also consider the effect of the instabilities on the phase difference (in degrees), ψ, between the inlet velocity fluctuations of the two flames. This is shown in fig. 9(d), with positive values defined as the left hand side injector leading the right hand side injector. The flames are approximately in phase with each other for all ϕ, with a maximum difference of $\approx 4°$. Slight differences in phase are again observed to depend on S. Between $0.8 > \phi > 0.9$ the right hand side flame response lags when the flames are merged, but leads for $S = 2.00D$. At present we do not have an explanation for why a small delay in p' between each flame occurs.

3.2. Characterisation of flame front events

In the previous section, a generalised approach for flame annihilation event tracking based on flame topology similar to Chen et al. [6] was presented as well as the amplitude and frequency response of self-excited twin flame configurations for different S. We now investigate the flame dynamics in more detail by characterising flame annihilation events in stable and self-excited conditions for different S using the flame front event tracking algorithm.

3.2.1. Stable flames

The annihilation event algorithm was initially applied to a case without significant self-excited oscillations ($\phi = 0.7$) in order to assess the effect of separation distance. Figure 10 shows coloured JPDF contours of FCC, PBO and CR events for $S = 2.00D$ and $1.14D$,
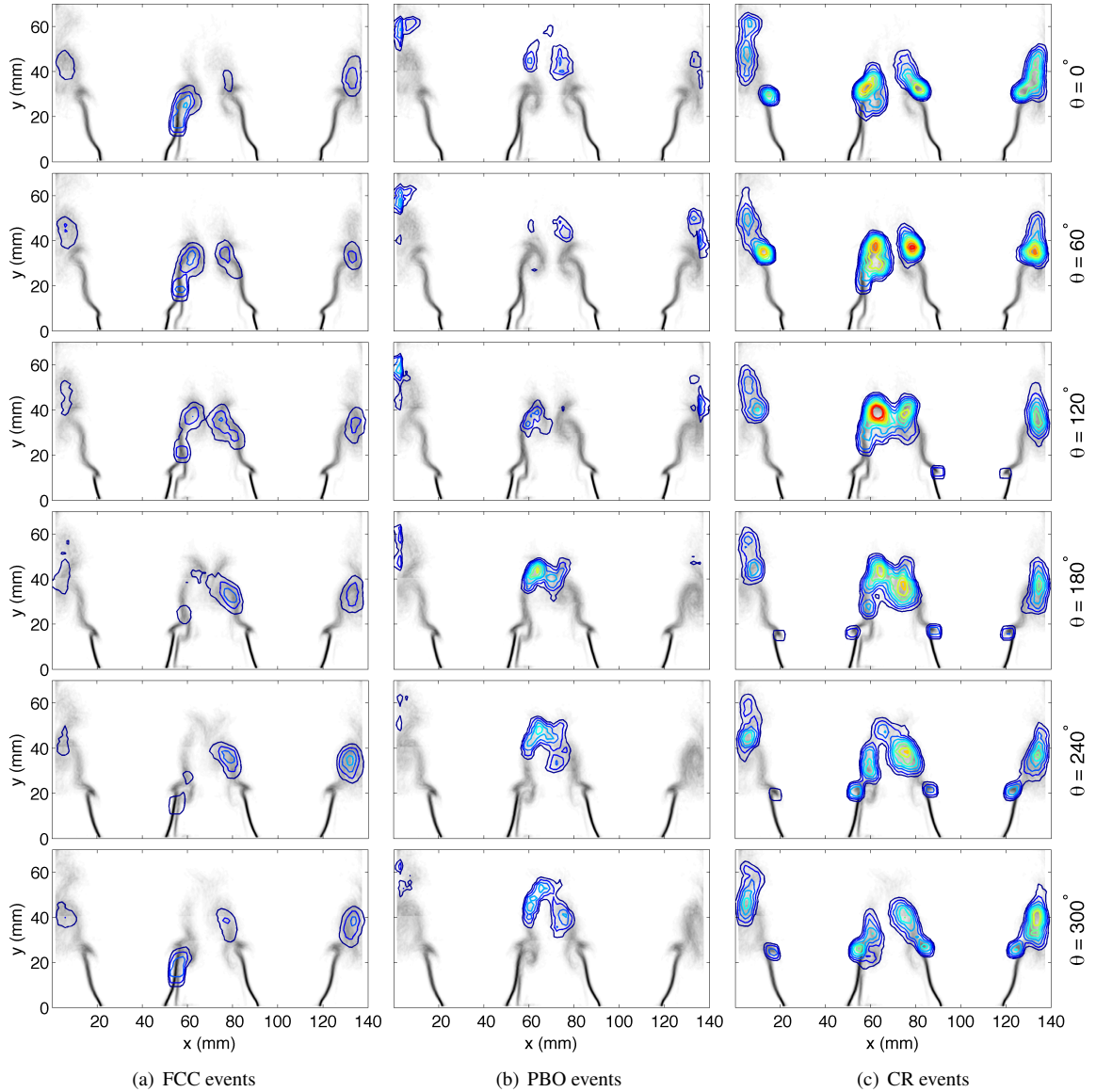
Figure 11: Phase averaged JPDF of different flame front events for self-excited case, $\phi = 0.8$, $S = 2.00D$. Probability densities for each column are indicated with the corresponding colour bar at the column head of fig. 12. The phase location in the oscillation cycle is shown on the right hand side. (*Colour online*).

plotted over the mean FSD distribution which is shown for context in grey scale. The JPDF represents the spatial distribution of event probability. Given that the flame dynamics are similar for the two closely spaced flame cases (shown in forced flames previously [20], and for the current flames in §3.2.2) for brevity only results from the $S = 1.14D$ and $S = 2.00D$ cases are presented.

For both S, the probability of FCC and PBO events occurring is significantly higher in the central interact-

ing region in comparison with the near wall regions. Given that these events occur when opposing flame fronts approach one another, the presence of a neighbouring flame (as opposed to wall) would be expected to increase the probability of such events. However, the increase in probability of FCC and PBO type events occurring in the interaction region are an order of magnitude higher compared to the wall. In comparison, cusp events are more evenly distributed between the wall and central interacting regions, although the peak probabil-
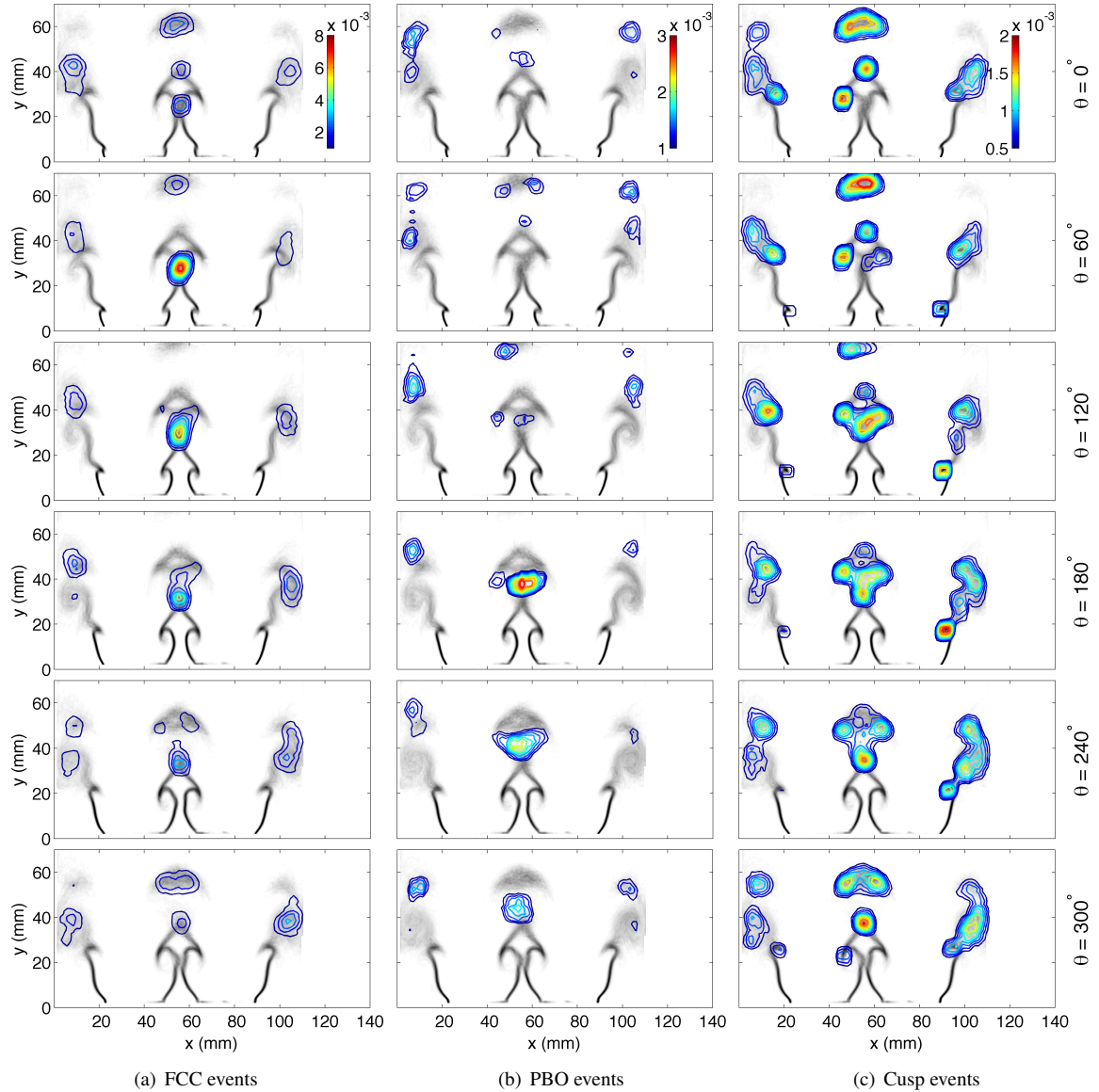
11

Figure 12: Phase averaged JPDF of different flame front events for self-excited case, $\phi = 0.8$, $S = 1.14D$. Probability densities for each column are indicated with the colour bar at the column head. The phase location in the oscillation cycle is shown on the right hand side. (*Colour online*).

ity still occurs in the latter.

In general, FCC events occur approximately 40mm downstream where the turbulent flame brush is more developed. For $S = 2.00D$ the highest probability of FCC events occurring is in the central interacting region towards the top of the flame brushes at $y \approx 55$mm. High probability of PBO occurs a little further downstream at $y \approx 65$mm and may extend further downstream outside the field of view. Furthermore, it is observed that pockets, albeit with low probability, are shed into the wake upstream of the interacting region. CR events on

the other hand show an overall lower range of probabilities than FCC and PBO events, but show peaks near the edges of the flame brushes where both flames interact and in the upstream wake of the interacting region.

The effect of flame merging on the probability distributions is shown at the top of fig. 10 for the $S = 1.14D$ case. Two main effects can be observed: First the probability of FCC events significantly increases and is more concentrated in the central interacting region; Second their most probable location has moved upstream to $y \approx 40$mm. PBO events also show a corresponding in-

crease downstream of the FCC event region noting that FCC events can in general be considered a precursor to PCO events [6, 7]. CR events also show a more compact region of high probability around the flame merging region whilst the wall side flames are unaffected. Overall, these results show that flame merging not only promotes a significant increase in probability of FCC, PBO and CR events in the merging region but also alters their spatial location and can potentially explain the observed frequency shift and change in delay between merged and unmerged response shown in figs. 9(b), 9(c).

3.2.2. Self-excited flames

We now consider the characteristics of flame annihilation events in self-excited flames. Figures 11 and 12 show coloured phase averaged JPDF contours of FCC, PBO and CR events for both unmerged ($S = 2.00D$) and merged ($S = 1.14D$) flames respectively, plotted over the phase averaged FSD distribution which is shown in grey scale. At the selected equivalence ratio the oscillation amplitudes are similar for all cases and therefore it is suitable for a comparison of events.

Before the events are discussed it should be noted from observation of the greyscale FSD contours that the flame dynamics are extremely similar to the forced flames studied in previous work [20]. Therefore, these dynamics will not be discussed in detail here. Crucially however, the FSD contours illustrate that the flame/vortex structure in the interacting region between adjacent flames is highly dependent on S. At $S = 2.00D$ the shear layers in the interacting region roll up separately, forming two pairs of counter rotating vortices which then collide approximately 1D downstream, resulting in large scale flame merging. However, for closely spaced flames, the shear layers combine together before rolling up into a single large vortex structure which pinches off generating large scale flame merging in its wake.

For $S = 2.00D$ in fig. 11(a), FCC events occur predominantly during the vortex-wall impingement and during the collision of the counter rotating vortex pairs in the central interacting region. In comparison with the stable case, the number of events near the walls and in the central interacting region are closer, due to the generation of counter-rotating vortex pairs at each shear layer, which produce flame surface annihilation events through vortex wall interactions near the walls and vortex collisions in the central interacting region. The asymmetric stabilisation of flame elements on the left hand side shear layer in the central interacting region results in asymmetry in the FCC JPDF, with the closely separated flame fronts generating a significant

increase in FCC events on this shear layer, due to vortex pair pinch-off. It should be noted that over a single oscillation cycle the fluctuation in the number of FCC events is relatively small, with only the asymmetric vortex pinch off in the central interacting region driving significant fluctuations.

Figure 11(b) shows that PBO events tend to occur further downstream, as pockets isolated during the FCC events burn-off. This therefore also introduces a phase delay between these events, with the peak number of PBO events occurring approximately half a cycle after the peak number of FCC events. The FCC event asymmetry also creates an asymmetric distribution of PBO events in the central interacting region. In comparison with the near wall region there is a significantly increased probability of PBO events occurring in the interacting region, as a result of flame brush fragmentation in this highly turbulent zone.

As expected the algorithm also identifies elongated regions of unburned reactants that are advected into the bluff body wakes as cusp recovery events, which can be seen trailing each vortex pair in fig. 11(c). Significant cusp formation can also be seen around the vortex-wall impingement region and as vortices collide in the central interacting region, due to the highly strained flow in these regions. While there are a significant number of cusp events, and these are highly localised at a number of points in the domain, the fluctuation in the number of events over the cycle is relatively small, and therefore these may not contribute significantly to the net production of heat release oscillations.

In comparison the closely spaced flames ($S = 1.14D$) are shown in fig. 12. While the number, location and cyclic variation of the near wall FCC, PBO and cusp events are reasonable similar to the $S = 2.00D$ case, the merged vortex dynamics in the centre produce significantly different distributions. As the merged vortex pair in the centre pinches off there is a very high probability of FCC events in the central region which are directly associated with the vortex pinch-off, peaking at $\theta \approx 60°$, as shown in fig. 12(a). The probability of FCC events occurring at this phase angle are approximately 4 times higher than in the $S = 2.00D$ case. Following pinch-off the isolated region of unburned reactants is advected upwards, with the concentration of FCC events following it suggesting a continuation of breakdown of this large unburned pocket.

The isolated region of unburned gases which is separated by the FCC events is too large to be classed initially as a PBO event by the current implementation of the algorithm, but as it burns-off and begins to breakdown into smaller structures, shedding a number

13

(a) $S = 2.00D$ Near wall regions (b) $S = 2.00D$ Central region (c) $S = 2.00D$ Full domain

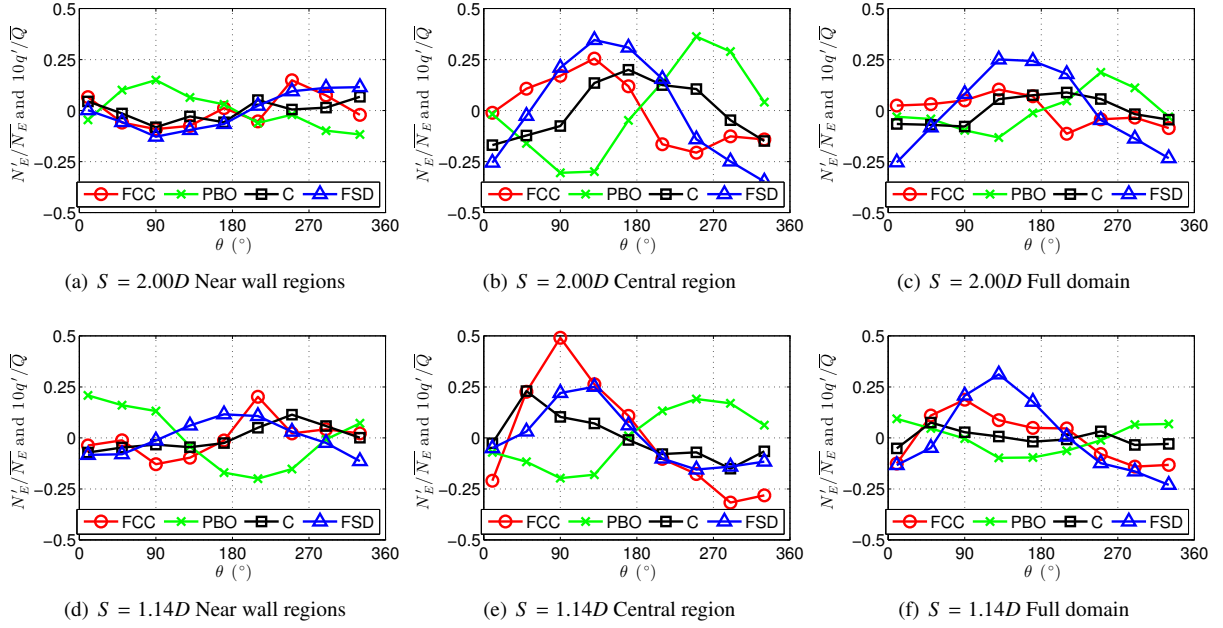(d) $S = 1.14D$ Near wall regions (e) $S = 1.14D$ Central region (f) $S = 1.14D$ Full domain

Figure 13: Phase averaged fluctuations of heat release and flame front event number for two self-excited cases for different parts of the imaging domain. $\phi = 0.8$. The fluctuations have been integrated spatially within each region of interest and normalised by their mean values.

of small pockets into its wake, as shown in fig. 12(b).

The formation of cusps is shown in fig. 12(c). In similarity with the widely spaced flames, significant cusp formation is observed as a result of the vortex roll up process. The larger merged central structure, results in very well defined cusp structures which are easy to track, and therefore not identified until later in the cycle (when they begin burning off rapidly). In addition to these cusp events, a significant number of additional events are seen in the wake of the merged vortex pinch-off process, and also following the isolated region of unburned reactants separated by the FCC events. This behaviour is somewhat expected, as FCC events are followed by cusp events, although the high probability of these rapidly burning regions following the central FCC event shows that additional heat release fluctuations may be generated by the rapid burn-off of these cusps, which again are a direct result of the merged pinch-off.

3.2.3. Globally integrated FSD

We now consider the temporal phasing of the events relative to the oscillation cycle in a more global sense by integrating the FSD and the annihilation events over selected areas of interest. Figure 13 shows the variation of the normalised integrated FSD ($10q'/\overline{Q}$) and normalised fluctuating number of FCC, PBO and cusp events ($N'_E/\overline{N_E}$) separated along the bluff body centre-

Event type	FCC	PBO	Cusp
stable ($\phi = 0.7$)			
S=1.14D	10	8.1	42.2
S=2.00D	12	6.2	49.6
self excited ($\phi = 0.8$)			
S=1.14D	9.2	13.5	30.8
S=2.00D	14.7	21.1	40.3

Table 1: Mean number of annihilation events over $t = 2.78$ms for the unforced flames, or 1 cycle for the self-excited flames

line positions into near wall regions, central interacting region, and their sum (as shown in fig. 2). The number of events have been normalised against their means and are presented in tab. 1. The integrated FSD has been multiplied by a factor of 10 to permit comparison using the same axis.

When S is large enough to ensure relatively isolated flames the fluctuations in the number of FSD and FCC and cusp events near the walls are low compared with the central interacting region, as shown in fig. 13(a). These annihilation events are in phase with the FSD fluctuations. The fluctuation in the PBO events is slightly larger, and approximately $180°$ out of phase with the other events, as these are generated following FCC events. When the flames are brought close together, similar near wall behaviour is observed (shown in fig. 13(d)), albeit with a slight phase shift.

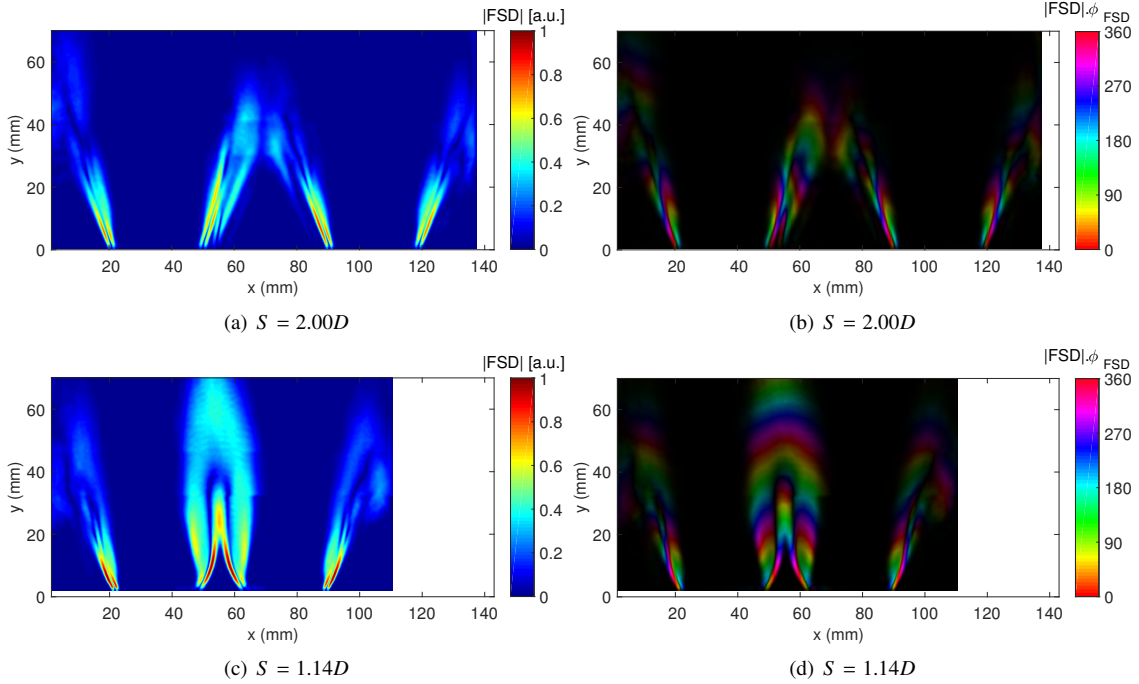It is noted from tab. 1 that self-excitation does not sig-

14

(a) $S = 2.00D$

(b) $S = 2.00D$

(c) $S = 1.14D$

(d) $S = 1.14D$

Figure 14: FSD fluctuating amplitude and amplitude weighted phase for two separation distances, $\phi = 0.8$. Frequencies are $f = 357Hz$ and $376Hz$ and amplitudes are $A = 0.092$ and 0.097 for the $S = 2.00D$ and $1.14D$ cases respectively. (*Colour online*).

nificantly change the total number of FCC events which occur, but rather modifies the phase at which they occur which is again consistent with the change in frequency and delay between merged and unmerged flames shown in figs. 9(b), 9(c). In the central region (fig. 13(b)) the number of FCC events peaks at $\theta = 135°$ after which they fall sharply. After the peak in number of FCC events, the following annihilation of flame surface area results in a decrease in FSD. The variation in PBO events is around $180°$ out of phase with the FCC events, increasing significantly as the number of FCC events fall. This is caused by increasing fragmentation of the flame front following FCC events. While tab. 1 shows that the number of PBO events does increase, again it is the timing of these events that is most notable in the self-excited flames, which show a clear dependence on phase.

When the flames are brought close together (fig. 13(e)) FCC events are increasingly concentrated at a single point in the cycle in the central region, due to the merged vortex pinch-off process, and the peak in the number of events is again shown to correspond to the FSD peak (fig. 13(e)). The peak number of events occurs slightly earlier than the $S = 2.00D$ case, with fluctuations peaking around $\theta = 90°$. Again the number of PBO events peaks $180°$ out of phase with the FCC

events which precede them.

The dominant response of the central region in terms of heat release fluctuations and number density of flame front events results in a similar phase distribution for the central region and the full domain (shown in fig. 13(c)). Therefore, in both merged and un-merged cases the peak number of FCC events are strongly correlated with the peak in FSD, providing supporting evidence that these events make a significant contribution to the non-linear flame response. This demonstrates a statistical link between the prevalence of annihilation events and the heat release oscillations in support of previous observations [3, 20].

Despite the strong correlation with event number, the total integrated magnitude of the FSD oscillations is similar irrespective of the separation distance between the flames. This is consistent with the similar global amplitude response observed previously in fig. 9(a). Therefore, in order to further quantify the link between event number and the flame surface area the size of the events may also have to be considered in future work.

3.3. Analysis of fluctuating heat release dynamics

In order to spatially relate the observed occurrence of annihilation events to the amplitude, phase and spatial

15

location of heat release fluctuations it is useful to analyse the weighted phase images. The spatial distribution of the fluctuating heat release can be assessed from figs. 14(a) and (c). For both S, significant fluctuations exist in the shear layers close to the flame base, where velocity oscillations cause the shear layer to flap at the frequency of self excitation. High fluctuation amplitude streaks are also observed on the bluff body side of the shear layers, as a result of the vortex induced advection of flame surface area into the bluff body re-circulation zones.

When $S = 2.00D$, the FSD fluctuation amplitudes in the interacting region shown in fig. 14(a)) are greater than those near the wall. This is particularly clear in the jet merging region at a downstream distance of around $y = 35$mm. Furthermore, this figure allows the spatial extent of the interacting region fluctuations to be clearly identified, with no significant fluctuations occurring above $y = 50$mm. Changing the flame separation distance is shown to significantly affect fluctuation amplitudes in the interacting region. As the flames are brought close together the amplitude of fluctuations increase significantly due to the enhanced vortex induced advection of flame surface area, and flame front merging in the wake of the pinched off vortex pair. The high amplitude peak between flames at approximately $y = 25$mm downstream in particular corresponds almost exactly to the most probable location of FCC events identified in the previous section. The statistical link between the annihilation events and the strong heat release oscillations at this location support the individual observations of such events preceding the rapid local destruction of flame surface area. Furthermore, the advection of reactants in the pinched off vortex pair modifies the spatial distribution of heat release, with significant fluctuations present in the interacting region above $y = 55$mm.

The weighted phase images in figs. (b) and (d) show how flame merging affects the mean phase of the fluctuating heat release. Each colour represents a phase angle and therefore regions that are the same colour are oscillating in-phase. The convective wavelength of the disturbances are shorter than the flame length, and therefore multiple disturbances simultaneously travel along the flame, whose phase is depicted by the regions of repeated colour along the flame brush.

For $S = 2.00D$ and the wall-side flame fronts for $S = 1.14D$, the transverse motions of the flame as it oscillates is shown by the two adjacent streaks on the shear layers at the flame base (pink to green) which are $180°$ out of phase with each other. In the $S = 2.00D$ case, the phase response of the near wall and interact-

ing regions are similar. The higher amplitude fluctuations in the central interacting region further downstream ($y \approx 35$mm) corresponds to vortex induced changes to the flame surface area and are in good agreement with the occurrence of peak FCC events which occur at $\phi_{FSD} \approx 120°$ as shown in fig. 13(b).

For $S = 1.14D$, a significant change in the phase response of the FSD occurs in the interacting region with a distinct inner phase structure which is out of phase with but bounded by a larger phase structure. The inner structure is associated with the peak FSD response and its phase relation to the outer structures is directly correlated with the merged roll-up of the vortex pair. The pinch-off of the vortex pinch is well correlated with the uniform phase established across the whole interacting region as shown in the larger phase structure above $y = 40$mm, which is absent in the $S = 2.00D$ case. This provides further evidence correlating the fluctuating heat release rate with the thermo-acoustic response in fig. 11 which describe the spatial and temporal characteristics of flame annihilation events.

4. Conclusions

The effect of separation distance on the self-excited oscillations of two neighbouring turbulent premixed flames was investigated in the present study. Pressure and global OH* measurements were used to characterise the self excited response, and high speed OH-PLIF was used to investigate the flame dynamics. A novel flame front tracking algorithm was implemented to quantify the number of flame front annihilation events which occur during the self-excited oscillations.

Previously, flame proximity has been found to affect flame structure and the nature of the flame-vortex interactions when subject to acoustic forcing, which in the latter case led to differences in the thermo-acoustic response. In the current paper both the frequency of the self excited oscillations and their stability were found to vary significantly with S. Analysis of the phase-averaged and instantaneous flame dynamics yielded a similar picture to the forced response; bringing the flames closer together causes the shear layers and flames in the interacting region to combine into a single jet. Bringing the flames closer resulted in a change to the self-excited frequency, and the onset of high amplitude instabilities at lower equivalence ratios.

Analysing the number and phase location of flame front annihilation events demonstrated that FCC events closely proceed the peak FSD in both far and closely separated flames, showing that these events are strongly correlated and likely drive the rapid production and then

destruction of flame surface. Different vortex dynamics in the central interacting region between the closely separated flames changes the location of FCC events in the cycle, which is responsible for the observed changes in the heat release phase and therefore the stability of the system. Therefore, while the number of events may not change significantly, the present work shows that during self-excitation, these events occur preferentially at certain spatial locations, and at certain points in the oscillation cycle. The quantification of event probability in this work represents an important step towards a more complete understanding of these important dynamical mechanisms, and one which will be built on in future work.

5. Acknowledgements

[1] A. P. Dowling, Nonlinear self-excited oscillations of a ducted flame, Journal of Fluid Mechanics 346 (1997) 271–290.

[2] T. Schuller, D. Durox, S. Candel, Self-induced combustion oscillations of laminar premixed flames stabilized on annular burners, Combustion and Flame 135 (2003) 525 – 537.

[3] R. Balachandran, B. Ayoola, C. Kaminski, A. Dowling, E. Mastorakos, Experimental investigation of the nonlinear response of turbulent premixed flames to imposed inlet velocity oscillations, Combustion and Flame 143 (2005) 37 – 55.

[4] M. Talei, M. J. Brear, E. R. Hawkes, Sound generation by laminar premixed flame annihilation, Journal of Fluid Mechanics 679 (2011) 194–218.

[5] M. Talei, E. R. Hawkes, M. J. Brear, A direct numerical simulation study of frequency and lewis number effects on sound generation by two-dimensional forced laminar premixed flames, Proceedings of the Combustion Institute 34 (2013) 1093–1100.

[6] J. Chen, T. Echekki, W. Kollmann, The mechanism of two-dimensional pocket formation in lean premixed methane-air flames with implications to turbulent combustion, Combustion and flame 116 (1999) 15–48.

[7] R. Griffiths, J. Chen, H. Kolla, R. Cant, W. Kollmann, Three-dimensional topology of turbulent premixed flame interaction, Proceedings of the Combustion Institute 35 (2015) 1341 – 1348.

[8] A. Haghiri, M. Talei, M. J. Brear, E. R. Hawkes, Sound generation by turbulent premixed flames, Journal of Fluid Mechanics 843 (2018) 29–52.

[9] W. L. Roberts, J. F. Driscoll, A laminar vortex interacting with a premixed flame: measured formation of pockets of reactants, Combustion and Flame 87 (1991) 245–256.

[10] P.-H. Renard, D. Thevenin, J.-C. Rolon, S. Candel, Dynamics of flame/vortex interactions, Progress in energy and combustion science 26 (2000) 225–282.

[11] K. Schadow, E. Gutmark, Combustion instability related to vortex shedding in dump combustors and their passive control, Progress in Energy and Combustion Science 18 (1992) 117 – 132.

[12] T. J. Poinsot, A. C. Trouve, D. P. Veynante, S. M. Candel, E. J. Esposito, Vortex-driven acoustically coupled combustion instabilities, Journal of Fluid Mechanics 177 (1987) 265–292.

[13] C. Külsheimer, H. Büchner, Combustion dynamics of turbulent swirling flame, Combustion and Flame 131 (2002) 70–84.

[14] A. Birbaud, D. Durox, S. Ducruix, S. Candel, Dynamics of confined premixed flames submitted to upstream acoustic modulations, Proceedings of the Combustion Institute 31 (2007) 1257 – 1265.

[15] P. Palies, D. Durox, T. Schuller, S. Candel, The combined dynamics of swirler and turbulent premixed swirling flames, Combustion and Flame 157 (2010) 1698 – 1717.

[16] N. A. Worth, J. R. Dawson, Self-excited circumferential instabilities in a model annular gas turbine combustor: Global flame dynamics, Proceedings of the Combustion Institute 34 (2013) 3127–3134.

[17] S. Candel, D. Durox, T. Schuller, Flame interactions as a source of noise and combustion instabilities, in: 10th AIAA/CEAS Aeroacoustics Conference, Paper, volume 2928, pp. 1444–1454.

[18] O. S. Graham, A. P. Dowling, A low-order modelling of ducted flames with temporally varying equivalence ratio in realistic geometries, in: ASME 2011 Turbo Expo, ASME, pp. 277–288.

[19] P. Palies, T. Schuller, D. Durox, S. Candel, Modeling of premixed swirling flames transfer functions, Proceedings of the Combustion Institute 33 (2011) 2967–2974.

[20] N. A. Worth, J. R. Dawson, Cinematographic OH-PLIF measurements of two interacting turbulent premixed flames with and without acoustic forcing, Combustion and Flame (2011).

[21] M. Hauser, M. Lorenz, T. Sattelmayer, Influence of transversal acoustic excitation of the burner approach flow on the flame structure, Journal of Engineering for Gas Turbines and Power 133 (2011) 041501.

[22] C. K. Law, Combustion physics, Cambridge University Press, 2006.